



# Study on the triaxial unloading creep mechanical properties and creep model of shale in different water content states

Bingyang Li<sup>1,2</sup> · Fengwei Yang<sup>1,2</sup> · Pengzhao Du<sup>1,2</sup> · Zhenhong Liu<sup>1,2</sup>

Received: 30 March 2022 / Accepted: 26 August 2022 / Published online: 15 September 2022  
© Springer-Verlag GmbH Germany, part of Springer Nature 2022

## Abstract

The mechanical properties of rock materials are strongly affected by water. To investigate the time-dependent mechanical properties of the rock under the combined effect of a water-rich environment and long-term loading, graded unloading creep tests are conducted on shale in different water content states to investigate the effect of water saturation coefficients on the creep mechanical properties. The results show that the creep deformation of shale is impacted by both the confining pressure and the saturation coefficient. The creep deformation increases with the increase of the unloading confining pressure. The radial transient creep and steady-state creep are more obvious under the same deviatoric stress, and the creep deformation is much more than the axial. The creep deformation, average creep rate, and creep duration at each level all increase as the water saturation coefficient rises. Based on the results of graded creep tests, a nonlinear viscoelastic-plastic unloading creep constitutive model (UCCM) was established. It has been verified that the UCCM can describe the creep deformation laws of shale with different water saturation coefficients. The impact of deviatoric stress and water saturation coefficient on creep deformation is then examined using this model. The results of the study can serve as a theoretical foundation for analyses of rock works' long-term stability in areas with plenty of water.

**Keywords** Shale · Water saturation coefficient · Unloading creep · Creep model

## Introduction

In engineering construction, rock mass properties are often weakened by the water environment, which leads to engineering disasters such as gushing water of tunnels, landslide, and dam foundation deformation (Iverson 2000; Hudson and Harrison 2000; Song et al. 2018; Lin et al. 2019). The effect of water on the mechanical characteristics of rock materials has been extensively investigated. The strength, deformation, and failure characteristics of clay soft rock are closely related to water content; the mechanical parameters may significantly be lowered with a small increase in water content. The loss of uniaxial compression strength and elastic modulus for some clay rocks can be as high as about 90% in the

saturated state (Hawkins and McConnell 1992; Reviron et al. 2009; Wong et al. 2016). In addition, the tensile strength, deformation modulus, and failure mode of most rocks are weakened by the influence of water content (Hashiba and Fukui 2015; Roy et al. 2017; Chen et al. 2019). The above studies have focused more on the effect of water on the conventional mechanical properties of rocks. However, there are few studies on the unloading creep mechanical properties of rock under water–rock action.

The creep mechanical properties of rocks have an important influence on the long-term stability and safety of engineering rock masses. Engineering experience shows that the deformation characteristics of rock masses after excavation have obvious time effects (Chigira 1992; Bovis and Evans 1996; Deng et al. 2009; Brantut et al. 2013). Some underground rock engineering is not destroyed immediately after the excavation is completed, but the surrounding rock collapses and destroys after a period of creep deformation. At present, the creep mechanical properties of rocks are often studied by means of laboratory creep tests. The initial rock creep tests were mainly uniaxial compression creep tests, which were carried out

✉ Fengwei Yang  
yangfw0624@163.com

<sup>1</sup> Yellow River Engineering Consulting Co., Ltd,  
Zhengzhou 450003, China

<sup>2</sup> Key Laboratory of Water Management and Water Security  
for Yellow River Basin, Ministry of Water Resources (Under  
Construction), Zhengzhou 450003, China

on sandstone, marble, andesite, and salt to obtain complete strain–time curves including the accelerated creep phase, and a creep equation was proposed to describe the whole creep process (Cruden 1970; Okubo et al. 1991; Boukharov et al. 1995; Yang et al. 1999). After that, some scholars studied the coupling effects of stress, water, and temperature on the transient creep, steady-state and accelerated creep during triaxial creep of rocks, and analyzed the variance of axial and lateral strains with time (Fu et al. 1999; Kinoshita and Inada 2006; Yang and Jiang 2010). In addition, Nadimi and Shahriar (2014) predicted long-term creep parameters and defined time-dependent characteristics of the bonding material. Jiao et al. (2013) conducted a long-term creep monitoring of engineering rock mass and obtained a relationship between rock displacements and time. Based on the creep test results of rock under different conditions, there are currently a number of nonlinear creep models that have been built to describe the entire creep process of rock. Based on the Mises yield criterion, Wang et al. (2016) proposed a viscous-elastic–plastic model to describe the creep process. By introducing the fractional derivative theory, the creep model reflecting the whole creep process of rocks under different conditions was established (Zhou et al. 2012; Chen et al. 2013; Wu et al. 2015). However, a key limitation of the fractional calculus method is the inability to describe the accelerated creep phase of geotechnical materials. Based on the theory of continuum damage mechanics, some scholars proposed to describe the accelerated creep phase of rocks by introducing damage factors into the creep model (Fabre and Pellet 2006; Nedjar and Roy 2012; Deng et al. 2016). Despite the recent improvements in creep models of rock materials, there is still no simple and universal model to describe the whole rock creep process.

Most of the current research results concern the creep of rocks under loading situations, and there are still few studies on the creep mechanical properties of hard and brittle shales under unloading conditions. In this paper, the unloading creep test was carried out on shale with different water saturation coefficients, and the variation of deformation with time was analyzed. Based on the test results, a nonlinear creep model that can describe the accelerated creep stage is established, and the rationality of the model is verified. The research results can provide a reference for the long-term stability analysis of engineering rock mass in a water-rich environment.

## Test overview

### Experimental material

The rock material used in the experiment was taken from the Yijiashan Tunnel of the Baoshen Expressway in Hubei Province. The rock material is the Silurian Luojiaping Formation sandy shale; it is light gray; the overall texture is uniform and dense; there are no visible defects in the specimen appearance. The density of specimens varied in the range of 2689.5 ~ 2753.9 kg/m<sup>3</sup>; the longitudinal wave speed ranged from 3659.1 to 3978.7 m/s, indicating that the specimens were homogeneous. In order to diminish the scattering due to the anisotropy between the specimens, the core was drilled in the same direction and then cut into a cylindrical specimen with a diameter of 50 mm and a height of 100 mm. All specimens were polished to make the end surfaces perpendicular to the longitudinal axis within 0.02 mm. Figure 1 shows the composition and structural features of shale.

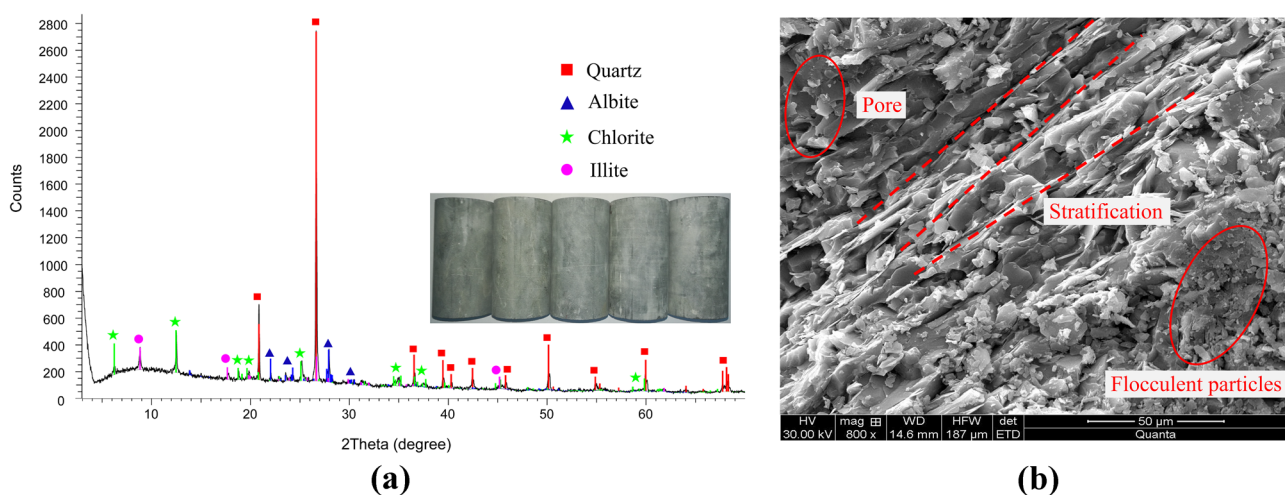


**Fig. 1** The mineral compositions and microscopic morphology of shale: **a** X-ray diffraction spectrum and **b** SEM micrograph

The mineral compositions of shale were measured with an X-ray spectrometer technique, and the test results are listed in Fig. 1a. The shale is mainly composed of quartz (45.5%), albite (20.5%), illite (18.9%), and chlorite (15.1%). The highest quartz content is about 45.5%, and the clay minerals illite and chlorite are about 34.0%. Both illite and chlorite minerals exhibit hydrophilic properties. Figure 1b shows the microscopic image obtained by SEM Quanta 250 at a magnification ratio of 800. It can be seen that there are micropores, cracks, flocculent particles, and other defects in the shale.

### Determination of water saturation coefficient

In this paper, specimens with different water saturation coefficients were prepared by natural soaking. First, the cylindrical specimens were dried for 24 h in the oven at a temperature of 110 °C (SL264-2007 2007). Subsequently, they were divided into 5 groups, and the weights of the dried specimens were measured after cooling to ambient temperature. Second, in addition to the dry specimen, the remaining 4 groups of specimens were placed in different containers, and then, water was injected every 2 h. After adding water four times, the specimens were completely submerged according to the standard measurement method (Li et al. 2019). Because of the good compact of the shale, the soaking times of four groups of specimens were determined to be 7 days, 14 days, 21 days, and 42 days, respectively. Finally, the water in the appearance of the specimen was wiped off, and the weight of the specimen was measured to determine the weight of water absorption when specimens were taken out. The specimens were coated with paraffin and wrapped with a waterproof membrane in time to prevent water loss.

The water content is determined by the increase in the weight of the specimen after water absorption, which is defined as

$$\omega_t = m_w/m_d \times 100\% \quad (1)$$

where  $\omega_t$  is the water content after  $t$  days of water absorption,  $m_w$  and  $m_d$  are the mass of water and dry specimen, respectively. The water content of the specimen is different under the same water absorption time. For example, after 42 days of water absorption, the water content ranges from 1.17% to 1.42%. Therefore, to unify the water content standard, the specimens of each group were normalized by the water content after immersion for 42 days. Define the water saturation coefficient  $w_s$  as

$$w_s = \omega_t/\omega_s \quad (2)$$

where  $\omega_s$  is the saturated water content.

### Test program

The creep test was conducted on a TFD-1500w triaxial rheological tester. The axial pressure is fixed during the unloading creep test, and the confining pressure is simultaneously released (fixed  $\sigma_1$ , reduced  $\sigma_3$ ). Considering the time-consuming characteristics of the creep test, for the same specimen, the number of unloading steps to obtain creep test curves with different deviator stress levels was increased. Determining the unloading confining pressure of 40 MPa, the number of unloading steps is 5~6. Considering that the rock generally enters the plastic yield stage at about 70% of the peak stress, the stress at the starting point of first step unloading is determined to be 70% of the triaxial peak stress. For example, for a dry sample, the conventional triaxial compressive strength at a confining pressure of 40 MPa is 278.2 MPa. Thus, the initial axial stress value is calculated to be around 195 MPa. The deviatoric stress at all levels of the unloading creep test is shown in Table 1.

Taking the dry specimen as an example, the specific steps of the creep test are as follows:

1. Loading the confining pressure  $\sigma_3$  and axial stress  $\sigma_1$  ( $\sigma_1 = \sigma_3$ ) simultaneously at a rate of 0.1 MPa/s until the confining pressure reaches a predetermined value of 40 MPa.
2. Keeping the confining pressure  $\sigma_3$  constant, continue to load the axial stress  $\sigma_1$  to 195 MPa at a rate of 0.1 MPa/s. Then, keeping the axial stress of 195 MPa constant, the first level creep test was started, and the specimen's strain value was recorded as the creep process progressed. The first level test is finished after the deformation is stabilized. The radial deformation must be less than 0.002 mm/24 h to meet the requirement for setting the deformation stability.
3. Gradually lowering the confining pressure  $\sigma_3$  to 30 MPa at a rate of 0.1 MPa/s, and then keeping the confining pressure ( $\sigma_3 = 30$  MPa) constant. The second-stage deviatoric stress creep test was started, and the deformation data of the specimen was recorded. By analogy, according to the scheme in Table 1, graded unloading of the confining pressure until the specimen is broken, the test is completed.

## Analysis of creep test results

### Creep deformation

The results of the shale's graded unloading confining pressure creep test are presented in Fig. 2. It can be seen that the creep deformation laws of specimens with different water saturation coefficients are the same. The creep strain at the starting point of unloading has a sudden change due

**Table 1** Deviatoric stress in triaxial unloading creep test of shale with different water saturation coefficients

Saturation coefficient $w_s$	No. grade	Initial confining pressure $\sigma_3 = 40$ MPa			$w_s$	No. grade	Initial confining pressure $\sigma_3 = 40$ MPa		
		Axial stress $\sigma_1$ (MPa)	Confining pressure $\sigma_3$ (MPa)	$\sigma_1 - \sigma_3$ (MPa)			Axial stress $\sigma_1$ (MPa)	Confining pressure $\sigma_3$ (MPa)	$\sigma_1 - \sigma_3$ (MPa)
0	1	195	40	155	0.2	1	175	40	135
	2	195	30	165		2	175	30	145
	3	195	20	175		3	175	20	155
	4	195	15	180		4	175	15	160
	5	195	10	185		5	175	10	165
	6	195	0	195		6	175	0	175
0.5	1	165	40	125	0.7	1	155	40	115
	2	165	30	135		2	155	30	125
	3	165	20	145		3	155	20	135
	4	165	15	150		4	155	15	140
	5	165	10	155		5	155	10	145
	6	165	0	165		6	155	0	155
1.0	1	140	40	100	1.0	4	140	15	125
	2	140	30	110		5	140	10	130
	3	140	20	120		6	140	0	140

to transient creep, and then gradually decreases with the increase of time and becomes stable. The last-step creep deformation is the largest before failure. During the creep test, decelerated creep deformation and steady-state creep deformation gradually appeared with the increase of time, whereas accelerated creep appeared before the specimen failure. Under each level of deviatoric stress, the radial creep deformation is larger than the axial, and the characteristics of the transient creep and steady-state creep of the radial creep curve changes are more obvious. This is because when the confining pressure is released, it is equivalent to generating tensile stress in the radial direction of the specimen, which makes the microcracks easier to expand in the radial direction.

The results of shale unloading creep tests are given in Table 2. As can be seen from the table, both axial and radial transient strains are generated at the moment of unloading confining pressure, and the radial strain is much larger than the axial. In the steady-state creep stage, when  $w_s$  is less than 0.5, the radial creep strain is significantly greater than the axial, basically more than 2 times the axial strain. When  $w_s$  is greater than 0.5, the radial creep strain is slightly greater than the axial. It indicates that after water absorption, the weakening effect of water on shale counteracts part of the unloading effect. The unloading creep is reduced to grade 4 when  $w_s$  is greater than 0.7, which was related to the weakening of the mechanical properties after shale water absorption. Throughout the creep process, the average creep rate in the radial direction is greater than that in the axial direction.

Figure 3 shows the variation of steady-state creep strain with the saturation coefficient for each graded deviatoric stress. Due to the weakening effect of water, the strain of saturated specimen at the time of damage is different from other specimens, which is convenient to display in the image, and the values attached near the diamond symbol ( $\blacklozenge$ ) in the figure are the actual test results. It can be seen that when the creep grade is 4, the average axial and radial creep strains increase with the increase of water saturation coefficients. When  $w_s$  is 0.5, the mean axial deformation increases abruptly, while the radial strain increases relatively smoothly, which is related to the presence of fracture penetration within the specimen that is conducive to expansion along the axial.

### Creep rate

The transient creep rates of the dried and saturated specimens during the test are given in Fig. 4. The transient creep rate is calculated by the slope of the line between two adjacent points of the creep curve. As can be seen, the transient creep at the beginning of unloading is larger due to the unloading effect, and the radial transient creep rate is up to  $0.3 \times 10^{-3}/h$ . After entering the steady-state creep stage, the creep deformation rapidly decreases, the creep deformation per unit of time is very small, and the radial steady-state creep rate at this time basically remains constant at about  $3.9 \times 10^{-6}/h$ . The peak creep rate at the unloading

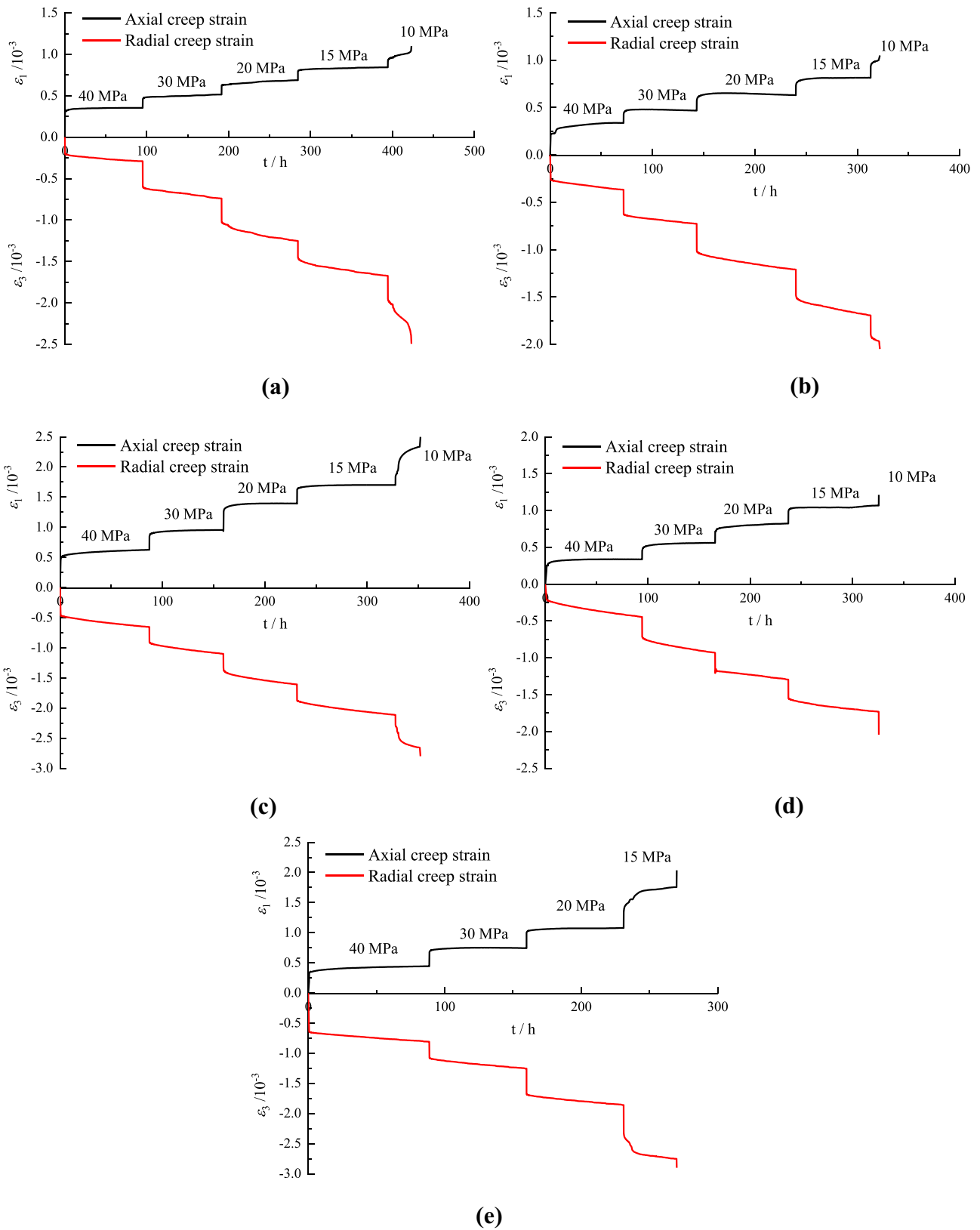


**Fig. 2** Strain–time curves of shale unloading creep tests under different water saturation coefficients: **a**  $w_s=0$ , **b**  $w_s=0.2$ , **c**  $w_s=0.5$ , **d**  $w_s=0.7$ , and **e**  $w_s=1.0$

**Table 2** Results of shale unloading creep tests under different water saturation coefficients

Saturation coefficient $w_s$	Stress			Transient creep		Steady-state creep		Average creep rate	
	$\sigma_3$ (MPa)	$\sigma_1$ (MPa)	$(\sigma_1 - \sigma_3)$ (MPa)	Axial $\epsilon_{ic1}/10^{-6}$	Radial $\epsilon_{ic3}/10^{-6}$	Axial $\epsilon_{sc1}/10^{-6}$	Radial $\epsilon_{sc3}/10^{-6}$	Axial $v_1/(10^{-6}/h)$	Radial $v_3/(10^{-6}/h)$
0	40	195	155	303.4	186.0	61.1	105.4	0.54	1.11
	30	195	165	93.1	307.9	67.1	140.5	0.70	1.46
	20	195	175	111.1	285.2	63.2	227.3	0.68	2.44
	15	195	180	104.1	200.5	54.3	220.9	0.60	2.45
	10	195	185	80.1	280.1	176.2	535.2	5.99	18.20
0.2	40	175	135	213.3	243.9	95.2	164.0	1.25	1.78
	30	175	145	92.1	260.4	69.1	145.2	0.68	1.62
	20	175	155	90.1	289.3	92.1	221.3	0.85	2.01
	15	175	160	83.1	281.1	84.1	232.5	1.11	2.78
	10	175	165	119.1	210.8	62.1	64.1	7.48	7.72
0.5	40	165	125	444.5	452.6	166.2	202.5	1.91	2.32
	30	165	135	155.3	256.3	153.1	216.9	2.06	2.99
	20	165	145	238.4	246.8	170.2	237.5	2.28	3.28
	15	165	150	185.9	264.5	202.4	258.8	2.08	2.69
	10	165	155	340.2	381.9	261.6	295.6	20.74	15.13
0.7	40	155	115	179.8	183.2	159.2	268.5	1.78	2.80
	30	155	125	112.2	274.8	204.3	246.9	2.75	3.27
	20	155	135	146.1	211.1	157.2	199.8	1.92	2.75
	15	155	140	141.2	200.1	182.3	242.9	2.06	2.67
	10	155	145	—	—	—	—	—	—
1.0	40	140	100	307.2	626.7	157.3	212.9	2.41	2.90
	30	140	110	231.3	269.2	182.1	196.7	2.16	2.74
	20	140	120	394.9	425.7	194.9	218.5	2.29	3.02
	15	140	125	386.3	477.4	420.6	435.1	10.81	10.67
	10	140	130	—	—	—	—	—	—

point is significantly higher than the rate at the steady-state creep stage. In addition, the radial steady-state creep rate of  $3.9 \times 10^{-6}/h$  is larger than the axial steady-state creep rate of

$2.1 \times 10^{-6}/h$ . The creep rate of saturated specimens is greater than that of dry specimens, and the creep rate of saturated specimens increases significantly before the destruction of

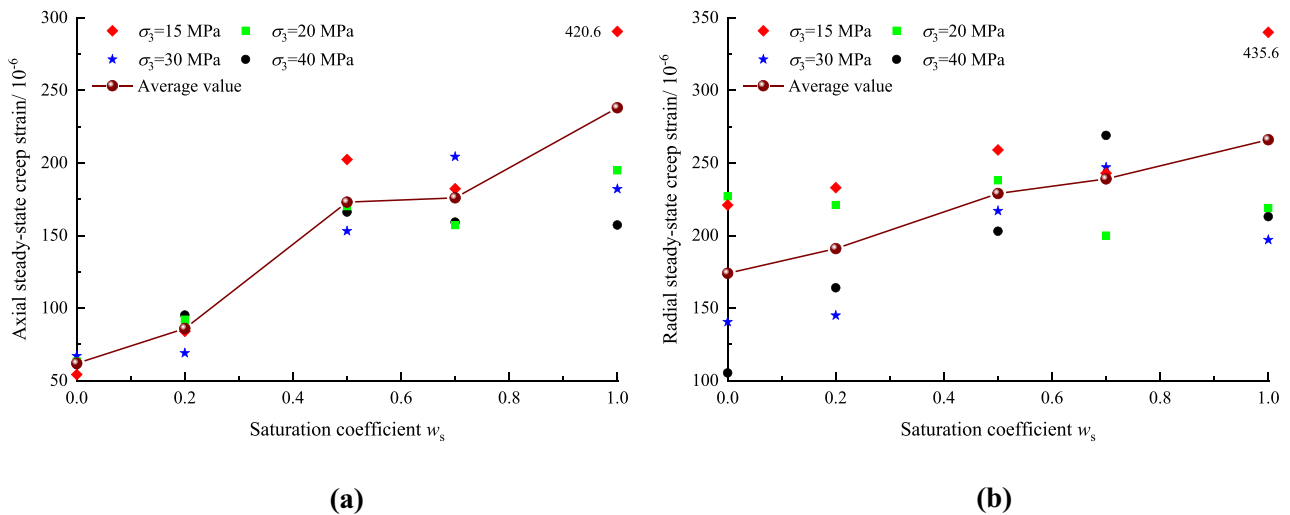


**Fig. 3** Variation of steady-state creep strain with saturation coefficient: **a** axial creep strain and **b** radial creep strain

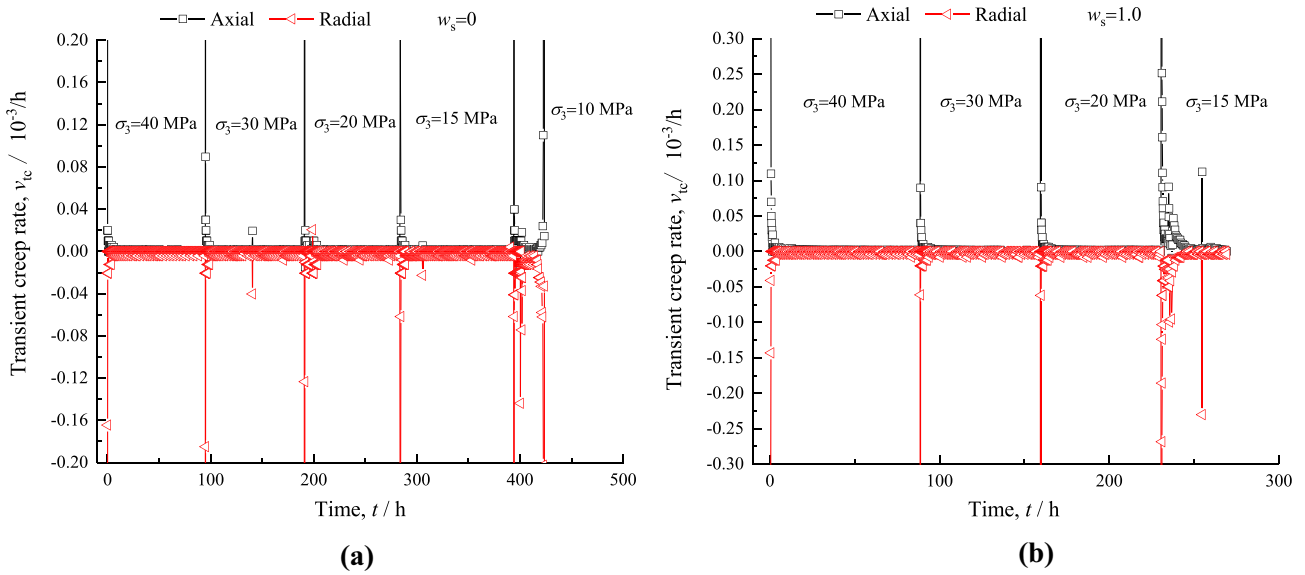


Fig. 4 Transient creep rate of shale with different water saturation coefficients: a  $w_s = 0$  and b  $w_s = 1.0$

specimens, corresponding to the dense increase of high rate creep points in the figure.

Figure 5 gives the average creep rate of unloading creep under different water saturation coefficients. The creep rate jumps up when the damage occurs, and the real test results are next to the diamond icon ( $\diamond$ ) to keep the graph coordinated.

The average creep rate increases with the increase of the saturation coefficient, and the increasing trend of the radial and axial average rate is the same. However, the average value of the radial creep rate is significantly greater than that of the axial. On the one hand, it indicates that the reaction between the clay minerals contained in the shale and

water reduces the bearing capacity of the internal skeletal structure and the way of cementation between the particles, resulting in a weakening of its ability to resist deformation. On the other hand, the total radial deformation increases more than in the axial direction as a result of the unloading effect. When the creep time is the same, the average creep rate in the radial direction is greater than the axial direction. When the water saturation coefficient is 0.5, the axial and radial average creep rates of shale are  $2.08 \times 10^{-6}/h$  and  $2.82 \times 10^{-6}/h$ . When the saturation coefficient is 0.7, the average creep rates in the axial and radial directions are  $2.12 \times 10^{-6}/h$  and  $2.87 \times 10^{-6}/h$ , respectively. The average creep rate is slightly increased relative to the saturation

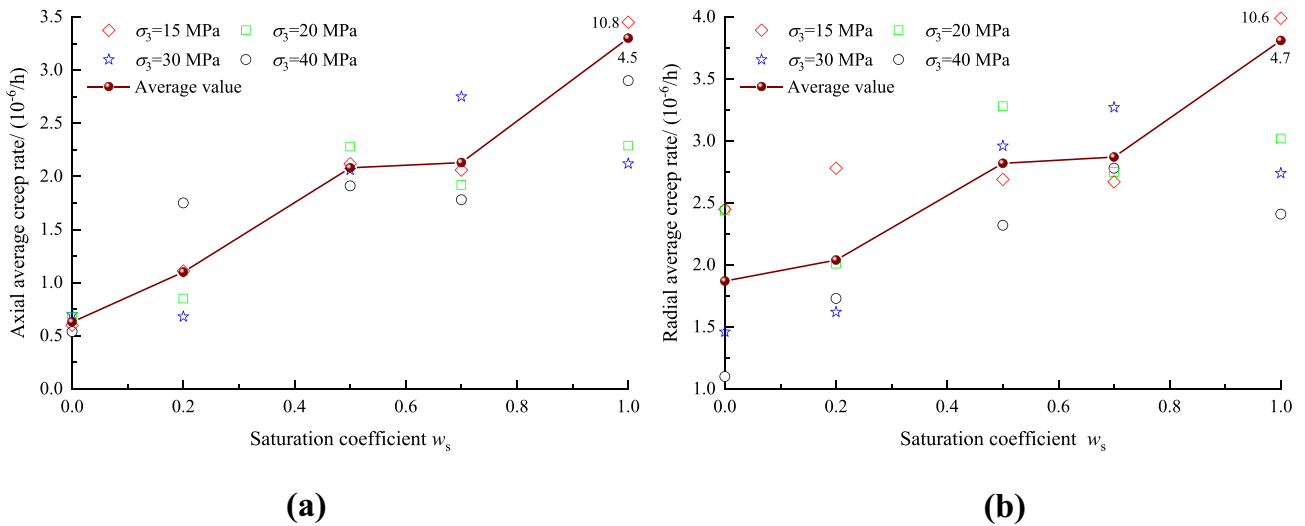


Fig. 5 Average creep rate of shale with different water saturation coefficients: a axial average creep rate and b radial average creep rate

coefficient of 0.5. This is related to the dense structure of the shale and the uneven distribution of water.

### Long-term strength

The determination of the long-term strength of the rock is important for the safety of the engineering rock mass. In this section, the long-term strength of the rock will be determined by the steady-state viscoplastic rate method. Figure 6 gives a schematic diagram of graded unloading creep. At low stress, the shale only undergoes viscoelastic deformation, and the steady-state creep deformation tends to be constant with time, while at high stress, the shale will undergo viscoelastic plastic deformation, and when the accumulated plastic deformation reaches a certain threshold, it will produce accelerated creep deformation leading to specimen damage, so the creep damage of the shale depends on the accumulation of plastic creep deformation at the steady-state creep stage (Cui and She 2011). Plastic creep deformation occurs when the viscoplastic rate is greater than 0, so the stress corresponding to the increase in viscoplastic rate from 0 during the steady-state creep phase of the rock can be used as the long-term strength of the rock.

For the unloading creep test, the steady-state creep phase radial creep deformation is greater than the axial, and the impact of unloading on the radial is greater than the axial. Therefore, the steady-state viscoplastic creep is calculated

using radial deformation as the object of study. Using the Boltzmann superposition principle, the graded unloading creep curve is transformed into a single-stage creep curve, and the radial single-stage creep curve of the dried specimen is given in Fig. 6b. The above analysis can determine the viscoplastic deformation and viscoplastic creep rate of the steady-state creep phase of the creep curve at different stress levels.

Under low stress, the rock generally produces transient elastic deformation and viscoelastic deformation, and the total strain can be expressed as

$$\Delta\epsilon = \Delta\epsilon_{ci} + \Delta\epsilon_{ce} \tag{3}$$

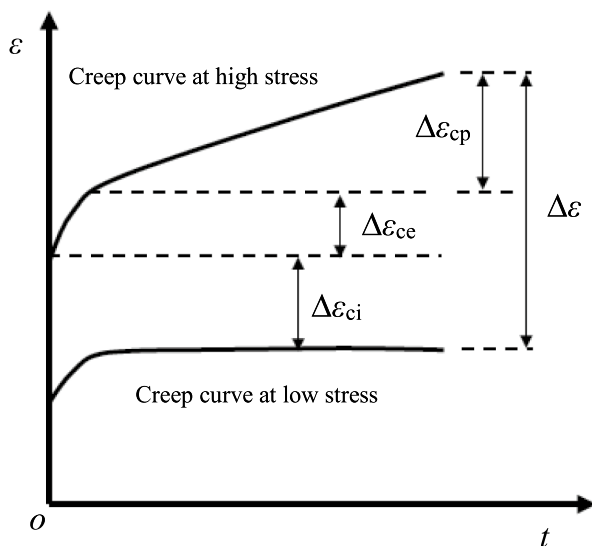
where  $\Delta\epsilon_{ci}$  and  $\Delta\epsilon_{ce}$  represent transient strain and viscoelastic strain, respectively.

Under high stress, the continuous loading action makes the microcracks within the rock expand and start sliding to produce the viscoplastic deformation. At this time, the total strain in the creep process should be expressed as

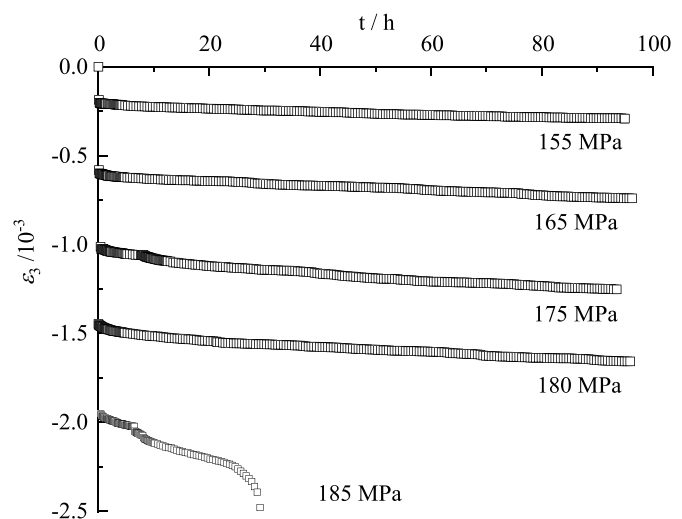
$$\Delta\epsilon = \Delta\epsilon_{ci} + \Delta\epsilon_{ce} + \Delta\epsilon_{cp} \tag{4}$$

where  $\Delta\epsilon_{cp}$  is the viscoplastic strain.

The viscoplastic creep strain can be obtained from the difference between the total strain and the instantaneous and viscoelastic strains. The viscoplastic creep rate is determined by the ratio of viscoplastic deformation to the corresponding time. Its specific calculation formula is as follows:



(a)



(b)

Fig. 6 Variation of single-stage creep curve with time: a schematic diagram of graded creep and b radial single-stage creep curve of the dried specimen



**Table 3** Steady-state viscoplastic creep rate of dry specimens at different stress levels

Confining pressure $\sigma_3$ (MPa)	Creep damage stress $(\sigma_1 - \sigma_3)$ (MPa)	Start time $t_1$ (h)	End time $t_2$ (h)	Start strain $\epsilon_{cp1}/10^{-3}$	End strain $\epsilon_{cp2}/10^{-3}$	Viscoplastic creep rate $v_{cp}/10^{-6}/h$
40	155	19.3	94.8	0.2486	0.2814	0.41
30	165	17.2	95.8	0.6406	0.7398	1.16
20	175	21.5	92.5	1.1243	1.2532	1.78
15	180	26.4	97.7	1.5509	1.7089	2.17
10	185	11.6	29.2	2.1326	2.3643	13.16

$$v_{cp} = \Delta\epsilon_{cp} / (t_2 - t_1) \tag{5}$$

where  $t_1$  and  $t_2$  are the starting time and ending time of the steady-state creep phase, respectively.

Table 3 gives the results of steady-state viscoplastic creep rate calculations for dry specimens at different stress levels. It can be seen that when the deviating stress is 185 MPa, the viscoplastic creep rate changes abruptly, and the creep deformation measured at this time is due to fissure extension penetration, which has a certain difference with the true value of viscoplastic creep. Therefore, in order to resolve the issue of viscoplastic deformation distortion brought on by fissure penetration, the creep rate at stresses 155–180 MPa was used for fitting to determine the long-term strength.

The steady-state viscoplastic creep rate at different deviatoric stresses and the fitted results are shown in Fig. 7. As can be seen, the steady-state viscoplastic creep rate varies almost linearly with the deviatoric stress, and the relationship between them can be described by the linear equation:

$$v_{cp} = 0.068(\sigma_1 - \sigma_3) - 10.284 \tag{6}$$

The long-term strength of the dry shale specimen can be determined by Eq. (6) as 151.2 MPa.

By the same method, the long-term strengths of the shale were determined to be 128.6 MPa, 116.4 MPa, 111.9 MPa, and 97.6 MPa for different water saturation coefficients. The ratio of long-term strength, which is determined by the steady-state viscoplastic creep rate method to creep damage stress, ranged from 0.751 to 0.817; plastic damage has occurred in some areas of the rock above this ratio.

Figure 8 illustrates the relationship between the long-term strength of shale and the water saturation coefficient. As can be seen, the long-term strength decreases as the water saturation coefficient increases; their variation law can be expressed with the following exponential equation:

$$\sigma_{Ls} = 87.4 + 62.1e^{-1.581w_s} \tag{7}$$

where  $\sigma_{Ls}$  is the long-term strength.

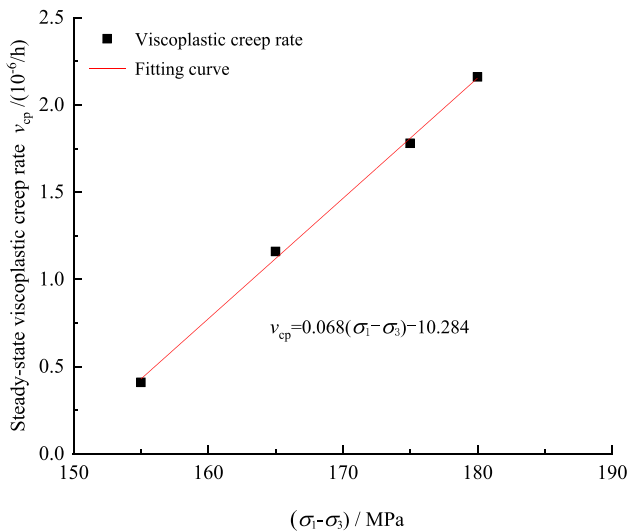


**Fig. 7** The relationship between steady-state viscoplastic creep rate and deviatoric stress

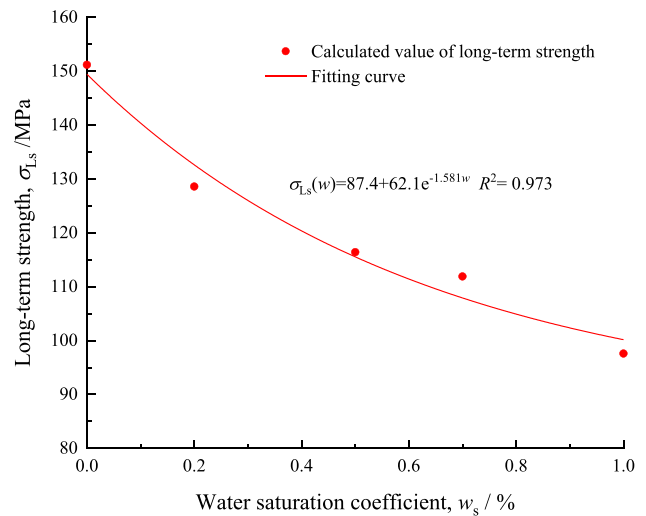


**Fig. 8** The relationship between water saturation coefficient and long-term strength

## UCCM of shale with different water saturation coefficients

### Establishment of the UCCM

The results of shale unloading creep test with different water saturation coefficients show that the creep deformation includes transient creep strain, steady-state creep strain, and accelerated creep strain. The Burgers model can describe the transient elastic deformation at the moment of loading and unloading, and the steady-state creep deformation under continuous loading, but it has no yield strength and cannot describe the accelerated creep deformation that occurs before rock failure (Shan et al. 2020). Therefore, it needs to be improved by connecting viscoplastic elements to establish a nonlinear UCCM with the effect of different water saturation coefficients.

Under the continuous action of high stress, the creep damage inside the rock material gradually accumulates with the increase of time, and the viscoelastic-plastic mechanical parameters will decrease with the increase of time in the creep process. Therefore, the variation of creep mechanical parameters with time is characterized by defining damage variables, and the damage evolution equation is constructed by introducing the damage variables into the component parameters to reflect the nonlinear creep deformation characteristics of the rock (Shao et al. 2003).

In recent decades, various experimental investigations have been conducted to characterize the damage evolution process (Krishnan et al. 2011; Wang et al. 2021). For example, the ultrasonic wave speed is related to the mechanical properties of a material; a drop of longitudinal wave speed usually represents a decrease in the elastic modulus of rock; the damage variable  $D$  can be estimated by (Hou 2003):

$$D = 1 - \frac{1}{1 + \epsilon_v} \frac{v_p}{v_0} \tag{8}$$

where  $\epsilon_v$  is the volumetric strain,  $v_p$  the ultrasonic wave speed, and  $v_0$  the initial wave speed.

Studies have shown that with the increase of creep time, the degree of damage gradually increases. Based on data of rock longitudinal wave velocity during the creep test, the accumulated damage variable  $D$  with time can be estimated in the form of negative exponential during the creep process, and its expression can be expressed as follows (Zhou et al. 2012):

$$D(t) = 1 - e^{-\alpha t} \tag{9}$$

where the parameter  $\alpha$  represents the damage accumulation rate and can reflect the degree of creep damage, as the value of  $\alpha$  increases, the rate of damage accumulation is accelerated and the damage deformation produced is greater. When  $t=0$ , the damage variable is zero, and when the rock specimen is damaged, the corresponding damage variable is 1.

The saturation coefficient of shale can indicate its initial damage degree. When the saturation coefficient is small, the weakening degree of shale is less affected by water, and the value of  $\alpha$  is small. When the saturation coefficient increases, the value of  $\alpha$  increases accordingly. By introducing the saturation coefficient  $w_s$  into the damage variable  $D$ , the expression of the damage variable under the combined effect of water weakening and time effect is obtained as follows:

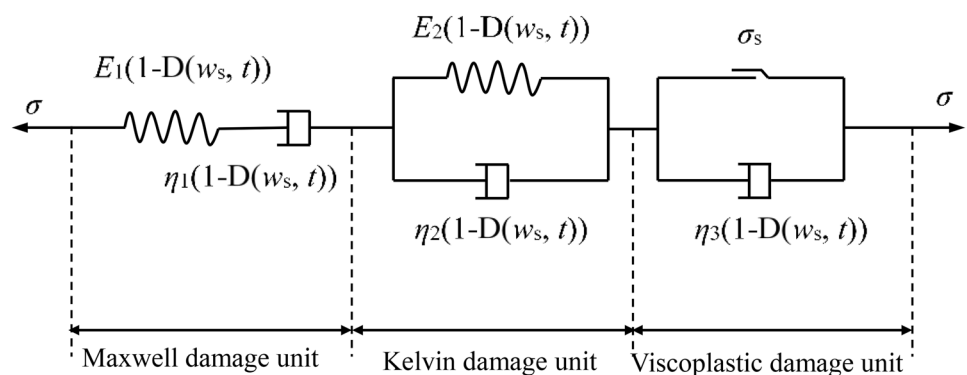
$$D(w_s, t) = 1 - e^{-\alpha(w_s)t} \tag{10}$$

where  $\alpha(w_s)$  can be obtained by fitting the experimental results.

Based on the above analysis, a nonlinear UCCM that reflects accelerated creep deformation is established by connecting the viscoplastic damaged unit with the Burgers creep model, and the combination of elements is shown in Fig. 9. The Burgers model consists of the Maxwell unit and the Kelvin unit. In the unloading creep process, it is assumed that the damage law of each component is the same as the increase of time. In Fig. 9, it can be seen that the total strain  $\epsilon$  of the UCCM is composed of three components:

$$\epsilon = \epsilon_{me}(w_s, t) + \epsilon_{ke}(w_s, t) + \epsilon_{vp}(w_s, t) \tag{11}$$

Fig. 9 Nonlinear unloading creep damage model of shale



where  $\epsilon_{me}$  is the viscoelastic strain corresponding to the Maxwell damage unit,  $\epsilon_{Ke}$  is the viscoelastic strain corresponding to the Kelvin damage unit, and  $\epsilon_{vp}$  is the viscoplastic strain corresponding to the viscoplastic damaged unit.

When the stress is greater than the long-term strength, the rock creep deformation will increase with time and produce accelerated creep deformation. Thus, the mechanical model describing the accelerated creep properties should contain specific components that can characterize the long-term strength. The viscous-plastic damage unit in Fig. 9 is formed by connecting the viscous pot unit in parallel with the plastic unit containing the stress switching function to respond to the accelerated creep phase properties. The creep equation of the viscoplastic damaged unit is

$$\epsilon_{vp}(w_s, t) = \frac{H(\sigma - \sigma_s)}{\eta_3 \exp(-\alpha(w_s)t)} t^n \tag{12}$$

where  $\eta_3$  is the viscosity coefficient,  $t$  is the creep time,  $\sigma_s$  is the long-term strength, and  $n$  is the fitting parameter reflecting the rapidity of creep in the accelerated creep phase of the rock.  $H$  is the switching function, whose expression is

$$H(\sigma - \sigma_s) = \begin{cases} 0 & \sigma \leq \sigma_s \\ \sigma - \sigma_s & \sigma > \sigma_s \end{cases} \tag{13}$$

Based on the above analysis, when the axial stress  $\sigma$  is less than the long-term strength  $\sigma_s$ , the model degenerates to the Burgers model with damage variables. Its corresponding equation is

$$\epsilon = \sigma \exp(\alpha(w_s)t) \left\{ \frac{1}{E_1} + \frac{t}{\eta_1} + \frac{1}{E_2} [1 - \exp(-\frac{E_2}{\eta_2}t)] \right\} \quad \sigma < \sigma_s \tag{14}$$

where  $E_1$  and  $E_2$  are the elastic modulus.  $\eta_1$  and  $\eta_2$  are the viscosity coefficients.

When the axial stress  $\sigma$  is greater than the long-term strength  $\sigma_s$ , the three parts of the damaged unit in Fig. 9 are involved in the creep process, at which time the creep equation of the shale is

$$\epsilon = \sigma \exp(\alpha(w_s)t) \left\{ \frac{1}{E_1} + \frac{t}{\eta_1} + \frac{1}{E_2} [1 - \exp(-\frac{E_2}{\eta_2}t)] \right\} + \frac{\sigma - \sigma_s}{\eta_3 \exp(-\alpha(w_s)t)} t^n \quad \sigma \geq \sigma_s \tag{15}$$

By combining Eqs. (14) with (15), the unloading creep equation for shale with different water saturation coefficients in one dimension is

$$\epsilon = \begin{cases} \sigma \exp(\alpha(w_s)t) \left\{ \frac{1}{E_1} + \frac{t}{\eta_1} + \frac{1}{E_2} [1 - \exp(-\frac{E_2}{\eta_2}t)] \right\} & \sigma < \sigma_s \\ \sigma \exp(\alpha(w_s)t) \left\{ \frac{1}{E_1} + \frac{t}{\eta_1} + \frac{1}{E_2} [1 - \exp(-\frac{E_2}{\eta_2}t)] \right\} + \frac{\sigma - \sigma_s}{\eta_3 \exp(-\alpha(w_s)t)} t^n & \sigma \geq \sigma_s \end{cases} \tag{16}$$

Rock mass is usually in a complex three-dimensional stress state, so it is necessary to establish the creep constitutive equation under a three-dimensional stress state. Based on the theory of elastoplastic, a one-dimensional creep constitutive equation can be extended to a three-dimensional equation. The following relations can be obtained:

$$\sigma_m = 3K\epsilon_m, \quad S_{ij} = 2Ge_{ij} \quad (i, j = 1, 2, 3) \tag{17}$$

where  $\epsilon_m$  is the first invariant of strain,  $\sigma_m$  is the first invariant of stress,  $S_{ij}$  is the deviatoric stress tensor,  $e_{ij}$  is the deviatoric strain tensor,  $K$  is the bulk modulus, and  $G$  is the shear modulus.

The relationship between the bulk modulus  $K$  and shear modulus  $G$  with the modulus of elasticity  $E$  and Poisson's ratio  $\nu$  is as follows:

$$G = \frac{E}{2(1 + \nu)}, \quad K = \frac{E}{3(1 + 2\nu)} \tag{18}$$

Based on Lemaitre's strain equivalence principle (Lemaitre 1985), by combining Eqs. (10) and (17), the strains of elastic damage unit with different water saturation coefficients under the three-dimensional stress state can be expressed as

$$\epsilon_{ij}^e = [\frac{1}{2G}S_{ij} + \frac{1}{3K}\sigma_m\delta_{ij}] \exp(\alpha(w_s)t) \tag{19}$$

where  $\delta_{ij}$  is the Kronecker function.

In the three-dimensional state, three-dimensional constitutive relation can be related to rock yield function  $F$  and plastic potential function  $Q$ . Assuming that the viscoplastic unit conforms to the associative flow rule ( $Q=F$ ) of the plastic yield theory. Hence, we adopt the Perzyna constitutive equation to express the three-dimensional constitutive relation for the strain of the damaged viscoplastic unit as (Perzyna 1966)

$$\dot{\epsilon}_{ij}^{vp}(w_s, t) = \frac{1}{\eta_3 \exp(-\alpha(w_s)t)} \left( \frac{F}{F_0} \right)^l \frac{\partial F}{\partial \sigma_{ij}} t \tag{20}$$

where  $F_0$  is a yield stress quantity used to normalize the yield function and  $l$  is the viscoplastic rate-sensitivity expo-

nent. For rock materials, assume that the initial yield stress quantity  $F_0=1$  and  $l=1$  (Abu Al-Rub et al. 2013). The yield

**Table 4** Parameter identification results of dry shale specimen under different deviator stress levels

$(\sigma_1 - \sigma_3)$ (MPa)	Type of strain	$K$ (GPa)	$G_1$ (GPa)	$G_2$ (GPa)	$\eta_1$ (GPa·h)	$\eta_2$ (GPa·h)	$\eta_3$ (GPa·h)	$n$	$R^2$
155	Axial	46.3	27.4	567.2	59,694.2	2712.1	201.2	0.021	0.966
	Radial	49.2	29.1	303.5	49,442.3	3992.9	308.8	0.029	0.994
165	Axial	71.6	36.9	456.7	55,444.1	3521.3	515.1	0.028	0.973
	Radial	53.6	27.6	206.4	15,396.6	2968.7	438.1	0.017	0.977
175	Axial	76.2	34.1	509.3	32,522.7	5426.5	672.1	0.059	0.984
	Radial	57.6	25.8	148.3	19,818.7	4680.1	410.5	0.061	0.995
180	Axial	55.7	23.2	169.5	35,267.3	2331.5	650.1	0.034	0.993
	Radial	48.5	20.2	412.9	12,987.1	3032.5	356.9	0.026	0.998
185	Axial	45.9	17.8	429.5	25,836.6	3678.5	696.1	0.006	0.952
	Radial	24.6	9.54	343.6	14,367.3	1111.2	359.2	0.013	0.962

function  $F$  is selected to satisfy the D-P criterion, and the relation is

$$F = \sqrt{J_2} - \sigma_m / \sqrt{3} \tag{21}$$

where  $J_2$  is the second invariant of the stress deviation tensor.

The laboratory rock mechanics test is a conventional triaxial test with  $\sigma_2 = \sigma_3$ , so Eqs. (17) and (21) can be simplified as

$$\sigma_m = \frac{1}{3}(\sigma_1 + 2\sigma_3), S_{11} = \sigma_1 - \sigma_m = \frac{2}{3}(\sigma_1 - \sigma_3), \sqrt{J_2} = (\sigma_1 - \sigma_3) / \sqrt{3} \tag{22}$$

From the above analysis, it can be obtained that the nonlinear unloading creep equation considering the influence of the saturation coefficient under conventional triaxial conditions is

$$\epsilon = \begin{cases} \exp(\alpha(w_s)t) \left( \frac{\sigma_1 + 2\sigma_3}{9K} + \frac{\sigma_1 - \sigma_3}{3G_1} + \frac{\sigma_1 - \sigma_3}{3\eta_1} t + \frac{\sigma_1 - \sigma_3}{3G_2} [1 - \exp(-\frac{G_2}{\eta_2} t)] \right) & \sigma_1 - \sigma_3 < \sigma_s \\ \exp(\alpha(w_s)t) \left( \frac{\sigma_1 + 2\sigma_3}{9K} + \frac{\sigma_1 - \sigma_3}{3G_1} + \frac{\sigma_1 - \sigma_3}{3\eta_1} t + \frac{\sigma_1 - \sigma_3}{3G_2} [1 - \exp(-\frac{G_2}{\eta_2} t)] \right) + \frac{\sigma_1 - \sigma_3 - \sigma_s}{3\eta_3 \exp(-\alpha(w_s)t)} t^n & \sigma_1 - \sigma_3 \geq \sigma_s \end{cases} \tag{23}$$

### Creep model parameter identification and model validation

At present, the commonly used method to obtain the creep model parameters is the damped least squares method (Yang and Cheng 2011). This method has been widely employed in the numerical analysis of engineering solutions because of its great application, precision, and ease of calculation. Therefore, based on the unloading creep test results of shale, this paper uses the damping least square method to identify

and analyze the parameters of the nonlinear creep model. During the fitting process, iterative optimization is repeated to improve the matching degree between the experimental data and the theoretical fitting curve as much as possible.

**Table 5** Parameter identification results of saturated shale specimen under different deviator stress levels

$(\sigma_1 - \sigma_3)$ (MPa)	Type of strain	$K$ (GPa)	$E_1$ (GPa)	$E_2$ (GPa)	$\eta_1$ (GPa·h)	$\eta_2$ (GPa·h)	$\eta_3$ (GPa·h)	$n$	$R^2$
100	Axial	31.8	23.3	142.5	39,073.5	1244.6	190.6	0.063	0.988
	Radial	21.1	15.5	486.2	40,455.5	2669.6	230.6	0.014	0.989
110	Axial	26.2	15.9	191.4	44,050.4	1418.7	203.7	0.016	0.969
	Radial	16.8	10.2	357.3	34,432.9	2773.1	136.2	0.011	0.985
120	Axial	43.4	21.7	305.5	21,280.6	1017.6	274.6	0.017	0.963
	Radial	14.6	7.3	295.8	11,249.9	1851.9	253.9	0.543	0.987
125	Axial	28.8	11.8	488.9	28,131.5	1060.5	230.3	0.175	0.976
	Radial	15.8	6.5	325.2	27,377.3	2109.8	174.3	0.148	0.987

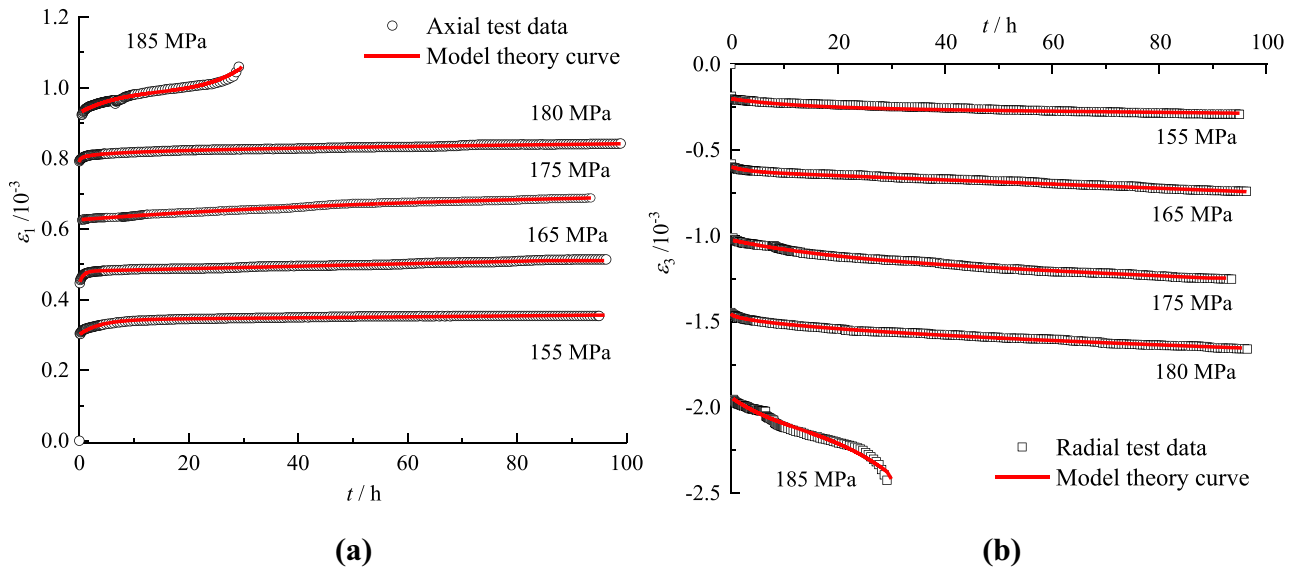


**Fig. 10** Comparison of dry specimen test data and fitting curve of nonlinear UCCM: **a** axial creep strain and **b** radial creep strain

By fitting the test data to the dried specimen, the value of  $\alpha_0$  is determined to be 0.0005/h for the creep phase. The value of  $\alpha(w_s)$  for other saturation coefficients can be obtained by the following equation:

$$\alpha(w_s) = \alpha_0(1 + w_s) \tag{24}$$

where  $\alpha_0$  is the value of the dried specimen.

The results of the parameter identification for the dried and saturated specimens are presented in Tables 4 and 5. The table shows that the identification results of the model

parameters are all different and there is no necessary connection between the parameters. This is related to the fact that rock creep parameters are nonconstant, varying with stress and creep time. There are differences in the internal structure of the rock, the distribution and quantity of microfractures, the instantaneous elastic deformation, and creep deformation produced by specimen under the same stress, and the creep parameters have a great difference.

The results of the parameter identification in Tables 4 and 5 were brought into the established creep model and

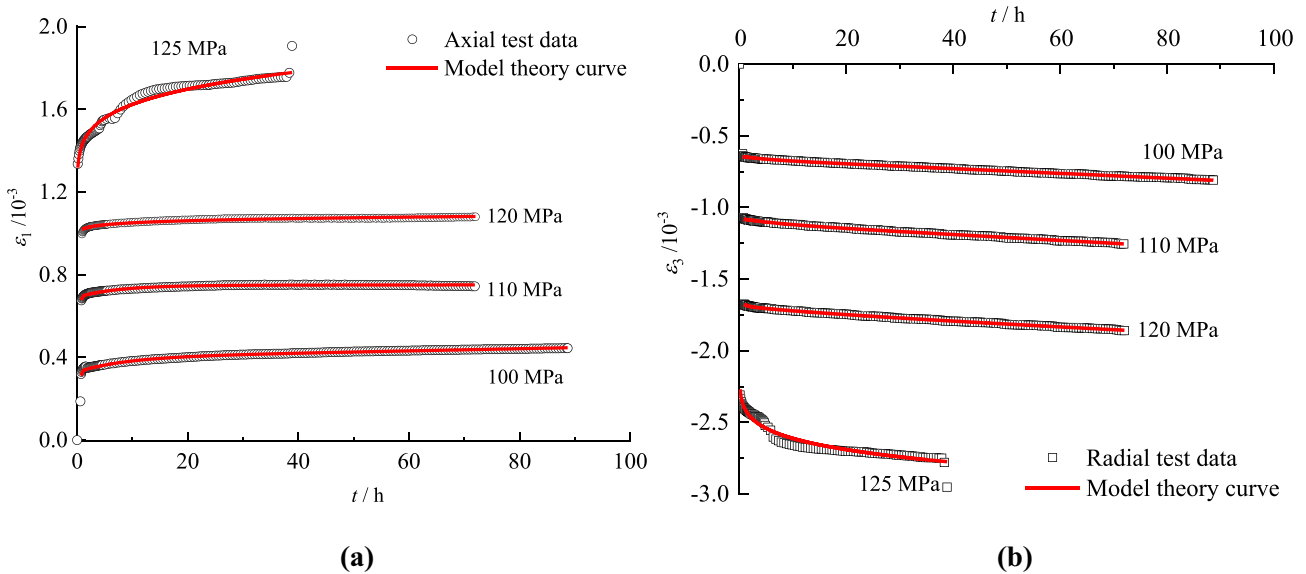


**Fig. 11** Comparison of saturated specimen test data and fitting curve of nonlinear UCCM: **a** axial creep strain and **b** radial creep strain

compared with the test results to obtain the theoretical creep curves of the dried and saturated specimens and the fitting results between the test data points, as shown in Figs. 10 and 11, respectively. It can be seen that the theoretical curves of the creep model can well fit the test results under each stress level, the correlation coefficients are above 0.95, and the proposed model is reasonable.

### Comparative analysis of two models and sensitivity analysis of the UCCM variables

This section will compare and analyze the Burgers model with the new model using test data to verify the rationality and validity of the new model. Figure 12 shows the fitting results of the Burgers model and the new model to the test data from the accelerated creep phase of the dried specimen. The fitting results of the two models to the experimental data were generally consistent in the initial stage; then, the fitting deviation of the burgers model from the experimental data increased, while the trend of the new model remained consistent with the experimental data. The new model describes the accelerated creep phase test data significantly better than the Burgers model. Therefore, the new model presented in this study is more suitable for describing the triaxial unloading creep properties of shale in different water content states.

Based on the creep parameter identification results and the new creep model, the effect of the two variables on the creep strain is compared and analyzed by changing the value of the deviatoric stress or the saturation coefficient. The creep mechanical parameters  $K=46.3$  GPa,  $G_1=27.4$  GPa,  $G_2=567.2$  GPa,  $\eta_1=59,694.2$  GPa·h,  $\eta_2=2712.1$  GPa·h,  $\eta_3=201.2$  GPa·h,  $n=0.021$  were selected for 155 MPa of deviatoric stress and brought into the creep model to calculate the creep deformation under different deviatoric or water saturation coefficients. The variation law of creep deformation with time for different deviatoric stresses or water saturation coefficients is given in Fig. 13.

It can be seen from Fig. 13a that the trend of the creep curve does not change when the deviatoric stress changes; the difference is that the transient and steady-state strain values increase slightly as the deviatoric stress increases, and it is easier to enter the accelerated creep phase. In Fig. 13b, when the deviatoric stress is constant, the slope of the steady-state creep curve becomes larger with the increase of the water saturation coefficients, and the steady-state creep strain increases significantly, and the larger the saturation coefficient, the more obvious this phenomenon. It indicates that the increase of saturation coefficient increases the damage degree of shale to a certain extent. The increase in deviatoric stress leads to an overall increase in creep deformation, while the saturation coefficient increases creep deformation due to the effect of the accumulation of damage on the creep rate during the creep process.

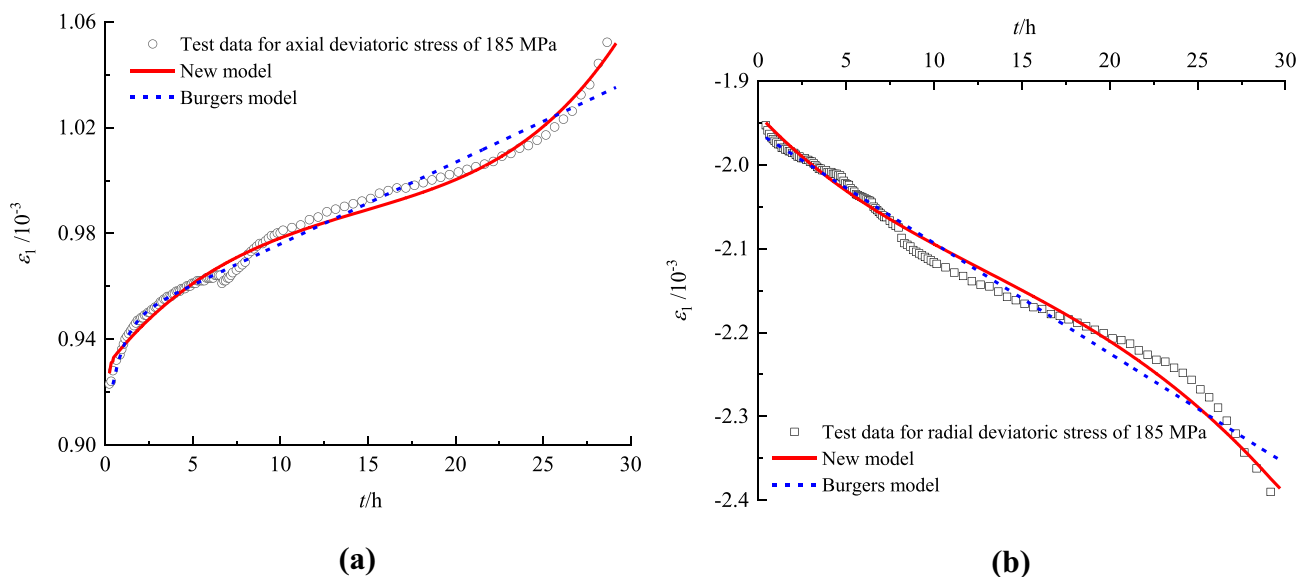


**Fig. 12** Comparisons of fitting results between the two models with test data: **a** axial and **b** radial

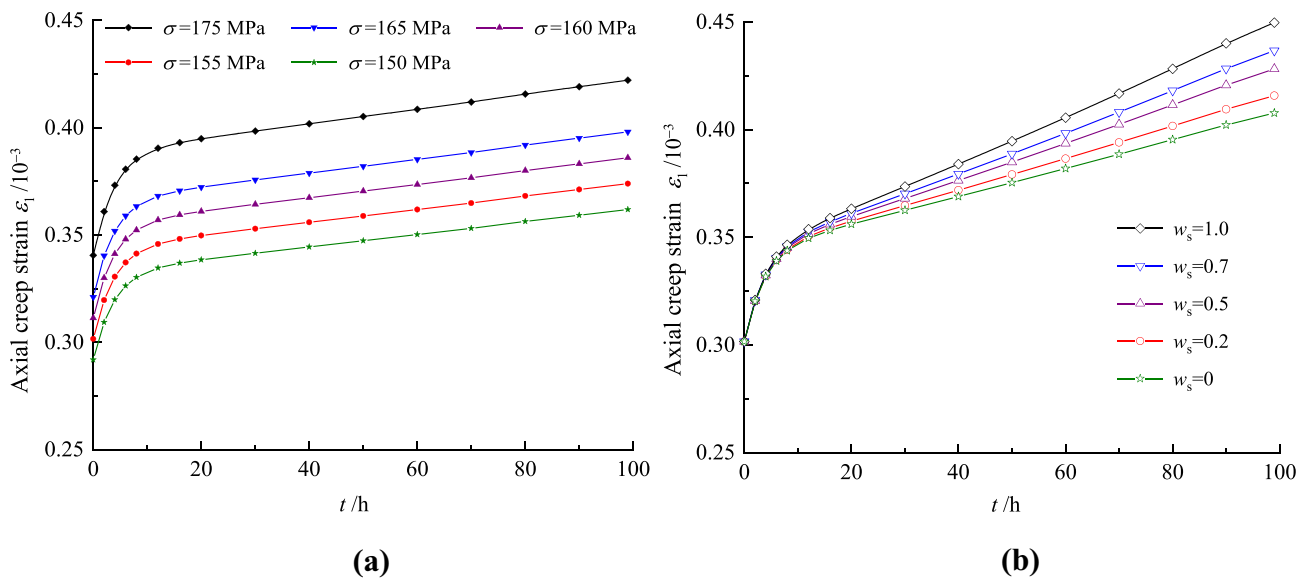


**Fig. 13** Theoretical creep curves at different variables: **a** creep curves at different deviatoric stress and **b** creep curves at different water saturation coefficients

### Conclusions

In this paper, graded unloading creep mechanical tests were carried out on shale specimens with different water saturation coefficients. Based on the experimental results, the variation law of creep mechanical parameters with water saturation coefficients was analyzed, a nonlinear UCCM was established, and the proposed model was then validated by comparison with the experimental results. The major research results are.

1. During the creep test, the steady-state creep deformation of shale with different water saturation coefficients is the smallest, but the time-consuming is the longest. The radial creep deformation is much greater than the axial deformation under different deviatoric stresses. When the creep test is in grade 4, the axial and radial average steady-state creep strains increase with the increase of water saturation coefficients. The average creep rate increases with the increase of the saturation coefficient. However, the average value of the radial creep rate under different water saturation coefficients is significantly greater than that of the axial. The increasing trend of the average creep rate is the same as the steady-state creep strain.
2. The long-term strengths determined by the steady-state viscoplastic creep rate decreased with the increase of the water saturation coefficients, and the ratios of the long-term strength to the creep damage stress were above 0.75; plastic damage has occurred in some parts of the specimen above this ratio.

3. Considering the effect of water weakening damage on the creep properties of rocks, a nonlinear viscoelastic UCCM is established. Compared with the experimental results, the fitted correlation coefficient is above 0.95, the established UCCM can better describe the creep deformation law of shale with time under different water saturation coefficients, and the proposed model is reasonable.

**Funding** This work is supported by the National Science and Technology Support Plan of China (No. 2020YFF0426370) and the Water Conservancy Technology Demonstration Project (No. SF-202010).

### Declarations

**Conflict of interest** The authors declare no competing interests.

### References

Abu Al-Rub RK, Darabi MK, Kim S et al (2013) Mechanistic-based constitutive modeling of oxidative aging in aging-susceptible materials and its effect on the damage potential of asphalt concrete. *Constr Build Mater* 41:439–454. <https://doi.org/10.1016/j.conbuildmat.2012.12.044>

Boukharov GN, Chanda MW, Boukharov NG (1995) The three processes of brittle crystalline rock creep. *Int J Rock Mech Min Sci Abs* 32:325–335. [https://doi.org/10.1016/0148-9062\(94\)00048-8](https://doi.org/10.1016/0148-9062(94)00048-8)

Bovis MJ, Evans SG (1996) Extensive deformations of rock slopes in southern Coast Mountains, Southwest British Columbia. *Canada Eng Geol* 44:163–182. [https://doi.org/10.1016/S0013-7952\(96\)00068-3](https://doi.org/10.1016/S0013-7952(96)00068-3)

Brantut N, Heap MJ, Meredith PG et al (2013) Time-dependent cracking and brittle creep in crustal rocks: a review. *J Struct Geol* 52: 17–43. <https://doi.org/10.1016/j.jsg.2013.03.007>

- Chen GQ, Li TB, Wang W et al (2019) Weakening effects of the presence of water on the brittleness of hard sandstone. *Bull Eng Geol Environ* 78:1471–1483. <https://doi.org/10.1007/s10064-017-1184-3>
- Chen H, Xu W, Wang W et al (2013) A nonlinear viscoelastic–plastic rheological model for rocks based on fractional derivative theory. *Int J Mod Phys B* 27(25): 5514–5518. <https://doi.org/10.1142/S021797921350149X>
- Chigira M (1992) Long-term gravitational deformation of rocks by mass rock creep. *Eng Geol* 32:157–184. [https://doi.org/10.1016/0013-7952\(92\)90043-X](https://doi.org/10.1016/0013-7952(92)90043-X)
- Chinese National Standard SL264–2007 (2007) Specifications for rock tests in water conservancy and hydroelectric engineering. The National Ministry of Water Resources of the People’s Republic of China, Beijing
- Cruden DM (1970) A theory of brittle creep in rock under uniaxial compression. *J Geophys Res* 75:3431–3442. <https://doi.org/10.1029/jb075i017p03431>
- Cui X, She CX (2011) Study of viscoplastic strain rate method to quickly determine long-term strength of rock. *Chin J Rock Mech Eng* 30:3899–3904
- Deng HF, Zhou ML, Li JL et al (2016) Creep degradation mechanism by water-rock interaction in the red-layer soft rock. *Arab J Geosci* 9:601. <https://doi.org/10.1007/s12517-016-2604-6>
- Deng QL, Zhu ZY, Cui ZQ et al (2009) Mass rock creep and land sliding on the Huangtupo slope in the reservoir area of the Three Gorges Project. *Yangtze River China Eng Geol* 58:67–83. [https://doi.org/10.1007/978-3-642-00132-1\\_15](https://doi.org/10.1007/978-3-642-00132-1_15)
- Fabre G, Pellet F (2006) Creep and time-dependent damage in argillaceous rocks. *Int J Rock Mech Min Sci* 43:950–960. <https://doi.org/10.1016/j.ijrmmms.2006.02.004>
- Fu J, Kiyama T, Ishijima Y (1999) Circumferential strain behavior during creep tests of brittle rocks. *Int J Rock Mech Min Sci* 36:323–337. [https://doi.org/10.1016/S0148-9062\(99\)00024-8](https://doi.org/10.1016/S0148-9062(99)00024-8)
- Hashiba K, Fukui K (2015) Effect of Water on the deformation and failure of rock in uniaxial tension. *Rock Mech Rock Eng* 48:1751–1761. <https://doi.org/10.1007/s00603-014-0674-x>
- Hawkins AB, McConnell BJ (1992) Sensitivity of sandstone strength and deformability to changes in moisture content. *Q J Eng Geol Hydrogeol* 25:115–130. <https://doi.org/10.1144/gsl.qjeg.1992.025.02.05>
- Hou ZM (2003) Mechanical and hydraulic behavior of salt in the excavation disturbed zone around underground facilities. *Int J Rock Mech Min Sci* 40:725–738. [https://doi.org/10.1016/S1365-1609\(03\)00064-9](https://doi.org/10.1016/S1365-1609(03)00064-9)
- Hudson JA, Harrison JP (2000) *Engineering rock mechanics—an introduction to the principles*. Elsevier, New York
- Iverson RM (2000) Landslide triggering by rain infiltration. *Water Resour Res* 36:1897–1910. <https://doi.org/10.1029/2000wr900090>
- Jiao YY, Wang ZH, Wang XZ et al (2013) Stability assessment of an ancient landslide crossed by two coal mine tunnels. *Eng Geol* 159:36–44. <https://doi.org/10.1016/j.enggeo.2013.03.021>
- Kinoshita N, Inada Y (2006) Effects of high temperature on strength, deformation, thermal properties and creep of rocks. *J Soc Mater Sci Jpn* 55: 489–494. <https://doi.org/10.2472/jsms.55.489>
- Krishnan B, Jitendra SV, Raghu VP (2011) Creep damage characterization using a low amplitude nonlinear ultrasonic technique. *Mater Charact* 62:275–286. <https://doi.org/10.1016/j.matchar.2010.11.007>
- Lemaître J (1985) A continuous damage mechanics model for ductile fracture. *J Eng Mater Technol* 107(1):83–89. <https://doi.org/10.1115/1.3225775>
- Li BY, Liu J, Bian K et al (2019) Experimental study on the mechanical properties weakening mechanism of siltstone with different water content. *Arab J Geosci* 12:656. <https://doi.org/10.1007/s12517-019-4852-8>
- Lin P, Li SC, Xu ZH et al (2019) Water inflow prediction during heavy rain while tunneling through karst fissured zones. *Int J Geomech* 19:04019093. [https://doi.org/10.1061/\(ASCE\)GM.1943-5622.0001478](https://doi.org/10.1061/(ASCE)GM.1943-5622.0001478)
- Nadimi S, Shahriar K (2014) Experimental creep test and prediction of long-term creep behavior of grouting material. *Arab J Geo sci* 7:3251–3257. <https://doi.org/10.1007/s12517-013-0920-7>
- Nedjar B, Roy RL (2012) An approach to the modeling of viscoelastic damage Application to the long-term creep of gypsum rock materials. *Int J Numer Anal Meth Geomech* 37:1066–1078. <https://doi.org/10.1002/nag.1138>
- Okubo S, Nishimatsu Y, Fukui K (1991) Complete creep curves under uniaxial compression. *Int J Rock Mech Min Sci Abs* 28:77–82. [https://doi.org/10.1016/0148-9062\(91\)93235-X](https://doi.org/10.1016/0148-9062(91)93235-X)
- Perzyna P (1966) Fundamental problems in viscoplasticity. *Adv Appl Mech* 9:243–377. [https://doi.org/10.1016/S0065-2156\(08\)70009-7](https://doi.org/10.1016/S0065-2156(08)70009-7)
- Reviron N, Reuschle T, Bernard JD (2009) The brittle deformation regime of water saturated siliceous sandstones. *Geophys J Int* 178:1766–1778. <https://doi.org/10.1111/j.1365-246X.2009.04236.x>
- Roy DG, Singh TN, Kodikara J et al (2017) Effect of water saturation on the fracture and mechanical properties of sedimentary rocks. *Rock Mech Rock Eng* 50:2585–2600. <https://doi.org/10.1007/s00603-017-1253-8>
- Shan RL, Bai Y, Ju Y et al (2020) Study on the triaxial unloading creep mechanical properties and damage constitutive model of red sandstone containing a single ice-filled flaw. *Rock Mech Rock Eng* 6:1–23. <https://doi.org/10.1007/s00603-020-02274-1>
- Shao JF, Zhu QZ, Su K (2003) Modeling of creep in rock materials in terms of material degradation. *Comput Geotech* 30:549–555. [https://doi.org/10.1016/S0266-352X\(03\)00063-6](https://doi.org/10.1016/S0266-352X(03)00063-6)
- Song K, Wang FW, Yi QL (2018) Landslide deformation behavior influenced by water level fluctuations of the Three Gorges Reservoir (China). *Eng Geol* 247:58–68. <https://doi.org/10.1016/j.enggeo.2018.10.020>
- FY Wang HW Huang ZY Yin et al (2021) Probabilistic characteristics analysis for the time-dependent deformation of clay soils due to spatial variability. *Eur J Environ Civ En* 1–19 <https://doi.org/10.1080/19648189.2021.1933604>
- Wang L, Liu Z, Zhuang Z (2016) Developing micro-scale crystal plasticity model based on phase field theory for modeling dislocations in heteroepitaxial structures. *Int J Plast* 81:267–283. <https://doi.org/10.1016/j.ijplas.2016.01.010>
- Wong LNY, Varun M, Liu G (2016) Water effects on rock strength and stiffness degradation. *Acta Geotech* 11:713–737. <https://doi.org/10.1007/s11440-015-0407-7>
- Wu F, Liu JF, Wang J (2015) An improved Maxwell creep model for rock based on variable-order fractional derivatives. *Environ Earth Sci* 73:6965–6971. <https://doi.org/10.1007/s12665-015-4137-9>
- Yang CH, Daemen JJK, Yin JH (1999) Experimental investigation of creep behavior of salt rock. *Int J Rock Mech Min Sci* 36:233–242. [https://doi.org/10.1016/S0148-9062\(98\)00187-9](https://doi.org/10.1016/S0148-9062(98)00187-9)
- Yang SQ, Cheng L (2011) Non-stationary and nonlinear visco-elastic shear creep model for shale. *Int J Rock Mech Min Sci* 48:1011–1020. <https://doi.org/10.1016/j.ijrmmms.2011.06.007>
- Yang SQ, Jiang YZ (2010) Triaxial mechanical creep behavior of sandstone. *Min Sci Tech* 20:339–349. [https://doi.org/10.1016/S1674-5264\(09\)60206-4](https://doi.org/10.1016/S1674-5264(09)60206-4)
- Zhou HW, Wang CP, Mishnaevsky L et al (2012) A fractional derivative approach to full creep regions in salt rock. *Mech Time-Depend Mater* 17(3):413–425. <https://doi.org/10.1007/s11043-012-9193-x>

Springer Nature or its licensor holds exclusive rights to this article under a publishing agreement with the author(s) or other rightsholder(s); author self-archiving of the accepted manuscript version of this article is solely governed by the terms of such publishing agreement and applicable law.